Unveiling a Chemisorbed Crystallographically Heterogeneous Graphene/ L10-FePd Interface with a Robust and Perpendicular Orbital Moment

Hiroshi Naganuma, Masahiko Nishijima, Hayato Adachi, Mitsuharu Uemoto, Hikari Shinya, Shintaro Yasui, Hitoshi Morioka, Akihiko Hirata, Florian Godel, Marie-Blandine Martin, et al.

ACSNANO

www.acsnano.org

ARTICLE

Unveiling a Chemisorbed Crystallographically Heterogeneous Graphene/$L1_0$-FePd Interface with a Robust and Perpendicular Orbital Moment

Hiroshi Naganuma,* Masahiko Nishijima, Hayato Adachi, Mitsuharu Uemoto, Hikari Shinya, Shintaro Yasui, Hitoshi Morioka, Akihiko Hirata, Florian Godel, Marie-Blandine Martin, Bruno Dlubak, Pierre Seneor, and Kenta Amemiya

Cite This: *ACS Nano* 2022, 16, 4139–4151

Read Online

ACCESS | Metrics & More | Article Recommendations | Supporting Information

ABSTRACT: A crystallographically heterogeneous interface was fabricated by growing hexagonal graphene (Gr) using chemical vapor deposition (CVD) on a tetragonal FePd epitaxial film grown by magnetron sputtering. FePd was alternately arranged with Fe and Pd in the vertical direction, and the outermost surface atom was identified primarily as Fe rather than Pd. This means that FePd has a high degree of $L1_0$-ordering, and the outermost Fe bonds to the carbon of Gr at the interface. When Gr is grown by CVD, the crystal orientation of hexagonal Gr toward tetragonal $L1_0$-FePd selects an energetically stable structure based on the van der Waals (vdW) force. The atomic relationship of Gr/$L1_0$-FePd, which is an energetically stable interface, was unveiled theoretically and experimentally. The Gr armchair axis was parallel to FePd $[100]_{L10}$, where Gr was under a small strain by chemical bonding. Focusing on the interatomic distance between the Gr and FePd layers, the distance was theoretically and experimentally determined to be approximately 0.2 nm. This shorter distance (≈0.2 nm) can be explained by the chemisorption-type vdW force of strong orbital hybridization, rather than the longer distance (≈0.38 nm) of the physisorption-type vdW force. Notably, depth-resolved X-ray magnetic circular dichroism analyses revealed that the orbital magnetic moment (M_l) of Fe in FePd emerged at the Gr/FePd interface (@inner FePd: M_l = 0.16 μ_B → @Gr/FePd interface: M_l = 0.32 μ_B). This interfacially enhanced M_l showed obvious anisotropy in the perpendicular direction, which contributed to interfacial perpendicular magnetic anisotropy (IPMA). Moreover, the interfacially enhanced M_l and interfacially enhanced electron density exhibited robustness. It is considered that the shortening of the interatomic distance produces a robust high electron density at the interface, resulting in a chemisorption-type vdW force and orbital hybridization. Eventually, the robust interfacial anisotropic M_l emerged at the crystallographically heterogeneous Gr/$L1_0$-FePd interface. From a practical viewpoint, IPMA is useful because it can be incorporated into the large bulk perpendicular magnetic anisotropy (PMA) of $L1_0$-FePd. A micromagnetic simulation assuming both PMA and IPMA predicted that perpendicularly magnetized magnetic tunnel junctions (p-MTJs) using Gr/$L1_0$-FePd could realize 10-year data retention in a small recording layer with a circular diameter and thickness of 10 and 2 nm, respectively. We unveiled the energetically stable atomic structure in the crystallographically heterogeneous interface, discovered the emergence of the robust IPMA, and predicted that the Gr/$L1_0$-FePd p-MTJ is significant for high-density X nm generation magnetic random-access memory (MRAM) applications.

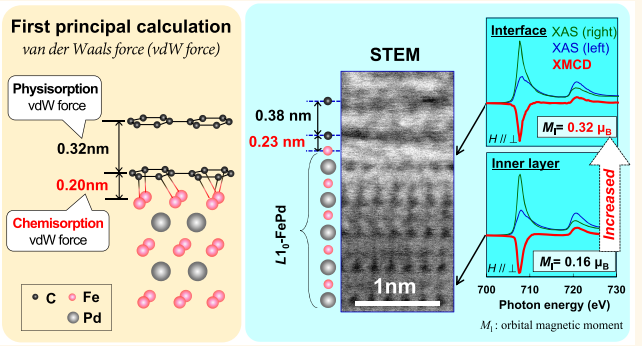

KEYWORDS: *$L1_0$ structure, FePd, graphene barrier, 2D, chemisorption interface, van der Waals force, interfacial perpendicular magnetic anisotropy*

INTRODUCTION

The spin injection/diffusion of two-dimensional (2D) systems in the in-plane direction has received considerable attention[1] owing to the long spin diffusion length afforded by π-bound conduction in 2D materials such as graphene (Gr).[2] The sources of spin injection into 2D systems are primarily metallic materials,

Received: November 11, 2021
Accepted: January 14, 2022
Published: February 28, 2022

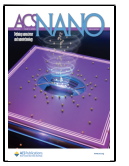

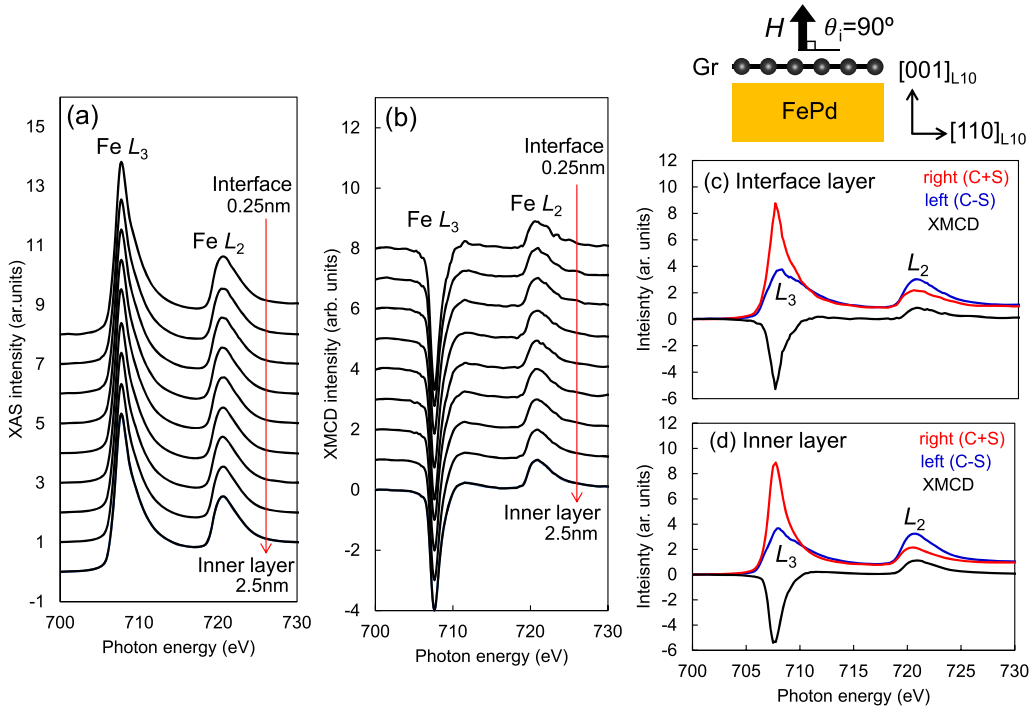

Figure 1. Fe L_3- and L_2-edge spectra with different λ ranging from 0.25 to 2.5 nm for $\theta_i = 90°$. A magnetic field was applied in the out-of-plane direction ($\theta_i = 90°$). (a) Depth profiles for an X-ray absorption (XAS) spectrum obtained by averaging right/left circularly polarized X-rays. (b) Depth profile of an X-ray magnetic circular dichroism (XMCD) spectrum obtained based on differences in circularly polarized XAS. XAS and XMCD spectra at the (c) interface and (d) inner layer.

resulting in intensive investigations of 2D/metal magnetic material systems for in-plane spin diffusion/conduction/conversion, which include gating,[3] the spin−orbit gap,[4] the Dzyaloshinskii−Moria interaction,[5] and the Rashba effect,[6−8] among others.[1,9] In contrast, studies on vertical spin conduction in 2D materials, such as magnetic tunnel junctions (MTJs), are scarce. Vertical spin conduction using 2D materials offers several attractive features. For example, according to theory, a large tunnel magnetoresistance (TMR) ratio was predicted for Co (or Ni)/Gr (or *h*-BN)/Co (or Ni) MTJs,[10−13] where 2D materials are tunneling barriers. Interfacial perpendicular magnetic anisotropy (IPMA) was induced in the Co/Gr (or *h*-BN)/Co interface *via* orbital hybridization of C_{pz}, Co_{dxy}, and $Co_{dx2-dy2}$.[13,14] Furthermore, the resistance−area (*RA*) product in the vertical direction in the Co/Gr/Co MTJ was reported to be small.[15] Large TMR ratios and IPMAs as well as a low *RA* product in the vertical direction in 2D materials benefit perpendicularly magnetized MTJs (p-MTJs) in nonvolatile magnetic random-access memory (MRAM). In the current industrial production, MRAM employs CoFeB/MgO p-MTJs[16] and their multiple layers; that is, $[CoFeB/MgO]_n$ p-MTJs.[17,18] $[CoFeB/MgO]_n$ p-MTJs afford high data retention by IPMA induced by the orbital hybridization of O_{pz} and Fe_{dz2},[19] as well as a high TMR ratio[20,21] induced by Δ_1 coherent tunneling.[22,23] The $[CoFeB/MgO]_n$ p-MTJs can be used until 1X nm generation MRAM, where 1X nm is the junction diameter of the p-MTJs. However, when setting a goal for ultra-high-density X-nm-generation MRAM, issues regarding the small *RA* product of the MgO barrier and the high thermal stability of the recording layer must be further considered. If the large bulk perpendicular magnetocrystalline anisotropy (PMA) of $L1_0$-ordered alloys[24] is combined with the IPMA and low RA product of 2D materials, the present issues can be mitigated. 2D materials (Gr, *h*-BN, MoS_2, WS_2, SnS, *etc.*) have hexagonal crystal symmetries, which are crystallographically heterogeneous against tetragonal $L1_0$-ordered alloys. To exploit tetragonal $L1_0$-ordered alloys having a large PMA,[24] the interface of "hexagonal 2D materials" and "tetragonal $L1_0$-ordered alloys" must be uncovered. Crystallographically heterogeneous hexagonal-2D materials and tetragonal-$L1_0$-ordered alloys provide an avenue for the further development of scaling in spintronics research in p-MTJs. However, reports of 2D materials combined with $L1_0$-ordered alloys are scarce. Large PMAs have been reported in many $L1_0$-ordered alloys.[24] Among them, $L1_0$-FePd[25] and $L1_0$-MnGa[26] have lower magnetic damping constants (α_{eff}). A small α_{eff} reduces the spin-transfer torque[27] switching current, which reduces the energy consumption during operation; hence, $L1_0$-FePd was used in this study. The aim of this study is to unveil the detailed interfacial atomic structure and IPMA of the crystallographically heterogeneous Gr/FePd interface using interface-specific analyses and describing a physical picture of a complex interface by comparing the experimental data with a first-principles calculation based on the van der Waals (vdW) force. Finally, the data retention characteristics were calculated by assuming an extremely small Gr/FePd recording dot (10 nm in diameter and 2 nm thickness) for high-density MRAM *via* micromagnetic simulation.

RESULTS AND DISCUSSION

The stacking structure of the sample is Gr/$L1_0$-FePd, where Gr is hexagonal and $L1_0$-FePd is tetragonal structures. Gr was grown by chemical vapor deposition (CVD), and $L1_0$-FePd (31 nm) was grown by radio frequency (r.f.) magnetron sputtering on the $SrTiO_3$(100) substrates.[28] The interfacial electric and magnetic properties were evaluated using fluorescence yield

https://doi.org/10.1021/acsnano.1c09843
ACS Nano 2022, 16, 4139−4151

depth-resolved soft X-ray absorption spectroscopy (XAS) and soft X-ray magnetic circular dichroism (XMCD) spectroscopy, respectively. The soft X-ray has an advantage for analyzing the interface with a Gr capping layer because a soft X-ray has a shallow penetration depth. Fe L_2- and L_3-edge XAS and XMCD spectra were measured to characterize the Fe states in the FePd layer. Figure 1 shows the $L_{2,3}$-edge spectra with different λ ranging from 0.25 to 2.50 nm. A magnetic field (H) was applied at $\theta_i = 90°$, which is in the perpendicular direction. The details of the measurement setup are explained in the Methods section. The XAS spectra were obtained by averaging the right and left circularly polarized X-rays (Figure 1a). The Gr/FePd bilayer sample was stored under atmospheric pressure and room temperature (RT) for more than one year. No peaks related to Fe oxidation were observed in the XAS, even when measured using high-intensity X-rays of high-energy synchrotron radiation, which is much higher than our previous X-ray photoelectron spectroscopy (XPS) measurements in the lab.[28] This result implies that Gr completely prevents the oxidation of FePd. The depth-resolved XMCD spectrum showed that the area ratio of the Fe L_2-edge was larger than that of the Fe L_3-edge from the inner layer to the surface layer (Figure 1b). The extracted spectra of the right/left circularly polarized XAS spectra and XMCD spectra at the interface and inner layer are shown in Figure 1c and d, respectively. Table 1 lists the spin magnetic moment (M_s), orbital magnetic moment (M_l), their summation ($M_{total} = M_s + M_l$), and their ratio (M_l/M_s) for the interface and inner layers. The magnetic parameters in Table 1 were deduced from the sum rule[29,30] by fitting the XMCD spectra of the interface and inner layers, respectively. The value of M_s of Fe in FePd, which is in contact with the Gr layer, was smaller than that at the inner layer. The decrease of M_s can be considered as a chemical bonding resulting from an orbital hybridization of Fe d-orbitals and C p-orbitals might have decreased M_{total}. In fact, it has been reported[31] that a decrease in M_s was experimentally observed at the interface between a hexagonal-Gr and 3-fold symmetry Ni bilayer. On the contrary, M_l of Fe in FePd was twice as large as that at the interface (@ inner: $M_l = 0.16\ \mu_B$ → @interface: $M_l = 0.32\ \mu_B$), and consequently, M_l/M_s at the interface was more than twice that at the interface (@inner FePd: $M_l/M_s = 0.06$ → @Gr/FePd interface: $M_l/M_s = 0.14$). Depth-resolved XMCD spectral analyses for $\theta_i = 90°$ revealed that M_s decreased and M_l of Fe in FePd was enhanced at the FePd/Gr interface.

The spin−orbit interaction in Gr was increased owing to the proximity effect upon contact with magnetic materials.[32−34] This spin−orbital coupling at the interface is expected to result in uniaxial magnetic anisotropy. Then, to clarify the emergence or not of IPMA, the anisotropic property of M_l was investigated by rotating H. Figure 2 shows the depth-resolved XAS and XMCD for $\theta_i = 30°$. $\theta_i = 30°$ represents H rotated by 30° from the in-plane direction. The geometry of θ_i can be confirmed in the Methods section. As shown in Table 1, M_s at the interface was smaller than that in the inner layer, which can be explained as same as that at $\theta_i = 90°$. It is noteworthy that M_l/M_s at the interface for $\theta_i = 90°$ is obviously larger than that at $\theta_i = 30°$ (@ Gr/FePd interface, 90°: $M_l/M_s = 0.14$ → 30°: $M_l/M_s = 0.09$). Classically, anisotropic M_l contributes to the uniaxial magneto-crystalline anisotropy energy (MAE). The uniaxial MAE can be described as $E(x) - E(z)$, where $E(x)$ and $E(z)$ are the MAEs to x- and y-axes, respectively. The relation between uniaxial MAE and anisotropic M_l is roughly described using the spin−orbit constant (ξ) as $E(x) - E(z) \cong \xi(M_l(z) - M_l(x))/4\ \mu_B$, where

Table 1. Spin Moment (M_s), Orbital Magnetic Moment (M_l), Their Summation ($M_{total} = M_s + M_l$), and Their Ratio (M_l/M_s) for Interface and Inner Layer Deduced by Fitting of XMCD Spectra Using Sum Rules[a]

$\theta_i = 90°$	M_s (μ_B)	M_l (μ_B)	M_{total} (μ_B)	M_l/M_s
Interface	2.3	0.32	2.62	**0.14**
Inner	2.7	0.16	2.86	**0.06**
$\theta_i = 30°$	M_s	M_l	M_{total}	M_l/M_s
Interface	1.1	0.11	1.21	**0.09**
Inner	1.7	0.11	1.81	**0.07**

[a]At $\theta_i = 90°$, the M_l/M_s at the interface was more than double that at the inner layer. M_l/M_s at $\theta_i = 90°$ was higher than that at 30°, indicating that there was anisotropy of the M_l in the perpendicular direction. The relatively small M_s at $\theta_i = 30°$ indicates that the external magnetic field was applied to the hard axis.

$M_l(x)$ and $M_l(z)$ are M_l for the x- and z-axes, respectively.[35] Thus, depth-resolved XMCD analyses from two directions (θ_i = 30° and 90°) uncovered that the IPMA emerged by perpendicularly anisotropic M_l at the FePd/Gr interface. A detailed discussion of the contribution ratio of M_l to IPMA by considering exchange splitting at the Fermi level[36] will be discussed separately.[37]

Figure 3 shows the fitting results of the depth dependence of M_s and M_l/M_s in Gr/FePd. To investigate the trends in M_s and M_l/M_s at the Gr/FePd interface, fitting was performed by assuming robust and gradual interfaces for $\theta_i = 90°$ and 30°, respectively. A gradual interface implies that the magnetic properties (M_s and M_l/M_s) at the interface change monotonically, whereas a robust interface implies that the magnetic properties change abruptly. The r-factor was calculated using the following formula:

$$r\text{-factor} = \mathrm{SQRT}\frac{\sum(\mathrm{exp} - \mathrm{sim})^2}{\sum(\mathrm{exp})^2} \quad (1)$$

where "exp" and "sim" are the experimental and simulated values, respectively. The r-factor reflects fitting accuracy, and a smaller r-factor indicates a better fit. The robust and gradual r-factors were 1.10% and 1.15%, respectively. From this fitting, either a robust or gradual interface can be interpreted; however, a robust interface makes the matching rate better.

To understand the perpendicularly anisotropic M_l that emerges at the interface, the interfacial structure in atomic resolution was investigated using cross-sectional scanning transmission electron microscopy (STEM) observations. In STEM observations, three different detectors were used to obtain the bright-field (BF), annular bright-field (ABF), and high-angle annular dark-field (HAADF) images; their acceptance angles were 0−10.1, 10.1−79.5, and 79.5−200.0 mrad, respectively (Figure 4a). It is advantageous to use various detectors simultaneously because the Gr/FePd bilayer is composed of "light" and "heavy" elements. Figure 4a shows a schematic illustration of the detector setup with the STEM diffraction patterns. The BF detector can most effectively visualize light elements owing to the low acceptance angle. However, the BF detector also includes unnecessary information

https://doi.org/10.1021/acsnano.1c09843
ACS Nano 2022, 16, 4139−4151

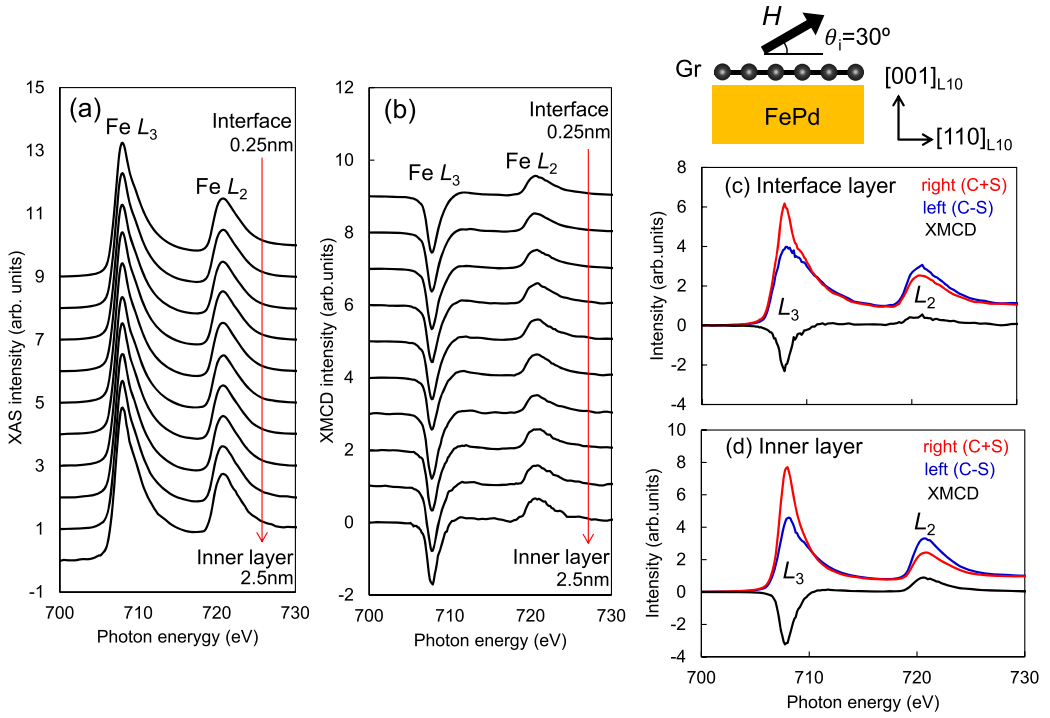

Figure 2. Depth-resolved (a) X-ray absorption (XAS) and (b) X-ray magnetic circular dichroism (XMCD) and typical spectra at the (c) interface and (d) inner layer. The magnetic field was rotated 30° from the in-plane direction (θ_i = 30°).

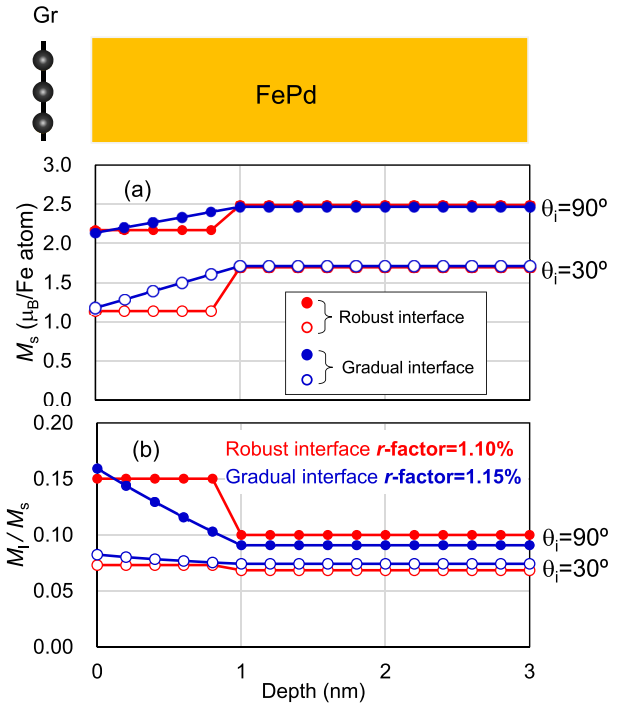

Figure 3. Fitting by the sum rule for depth-resolved X-ray magnetic circular dichroism (XMCD) spectra. (a) M_s and (b) M_l/M_s of Gr/FePd. The fitting was performed for the robust and gradual interfaces for θ_i = 90° and 30°.

such as lattice fringes and Fresnel fringes caused by the interference between the transmitted and diffracted waves. In addition, the contrast in the BF-STEM image was frequently inverted owing to the dynamic diffraction effect and phase-contrast transmission characteristics. Although annular detectors remove unnecessary information, the brightness of the images slightly decreases. The BF detector effectively visualizes light elements, and the annular detector effectively visualizes light and heavy elements; both detectors are necessary for observing the Gr/FePd bilayer. In the case of the annular detector, the ABF-STEM can accurately visualize carbon in Gr and HAADF-STEM can accurately visualize the position of heavy elements of Fe and Pd in FePd. Optimal observation parameters such as focusing/acceleration-voltage/astigmatism exist in each detector; here, the observation conditions are in between. STEM images for the electron incident direction of $[110]_{L10}$ are shown in Figure 4b and c. In the ABF-STEM images shown in Figure 4b and c, dark dots exist as indicated by the dashed orange arrows. These dots disappeared in the HAADF-STEM images, indicating that the dark dots in the ABF-STEM image represent carbon in Gr. The HAADF-STEM image of heavy elements confirmed the presence of Fe and Pd atoms in the FePd layer, which were arranged alternately in the perpendicular direction (Figure 4b and c). This highly alternating arrangement of Fe and Pd atoms results in a high degree of $L1_0$-ordering, which induces the high bulk PMA. The surface layer of FePd was obscure in the HAADF-STEM image, as shown in Figure 4b and c; hence, the contrast was adjusted to visualize the interface on the FePd side (Figure 4d). As a result, it was discovered that the outermost surface atom of FePd was identified primarily as Fe rather than Pd. Fe termination is beneficial because, in an Fe-based $L1_0$-ordered alloy, it was observed that the TMR ratio was higher when Fe, instead of a precious metal, was terminated at the interface.[38] The interatomic distances of the Gr and FePd layers were evaluated by line profiles in the out-of-plane direction. Figure 4e shows the line profiles from the dashed square area marked in Figure 4b. The distance between the outermost Fe layer in FePd and the

https://doi.org/10.1021/acsnano.1c09843
ACS Nano 2022, 16, 4139−4151

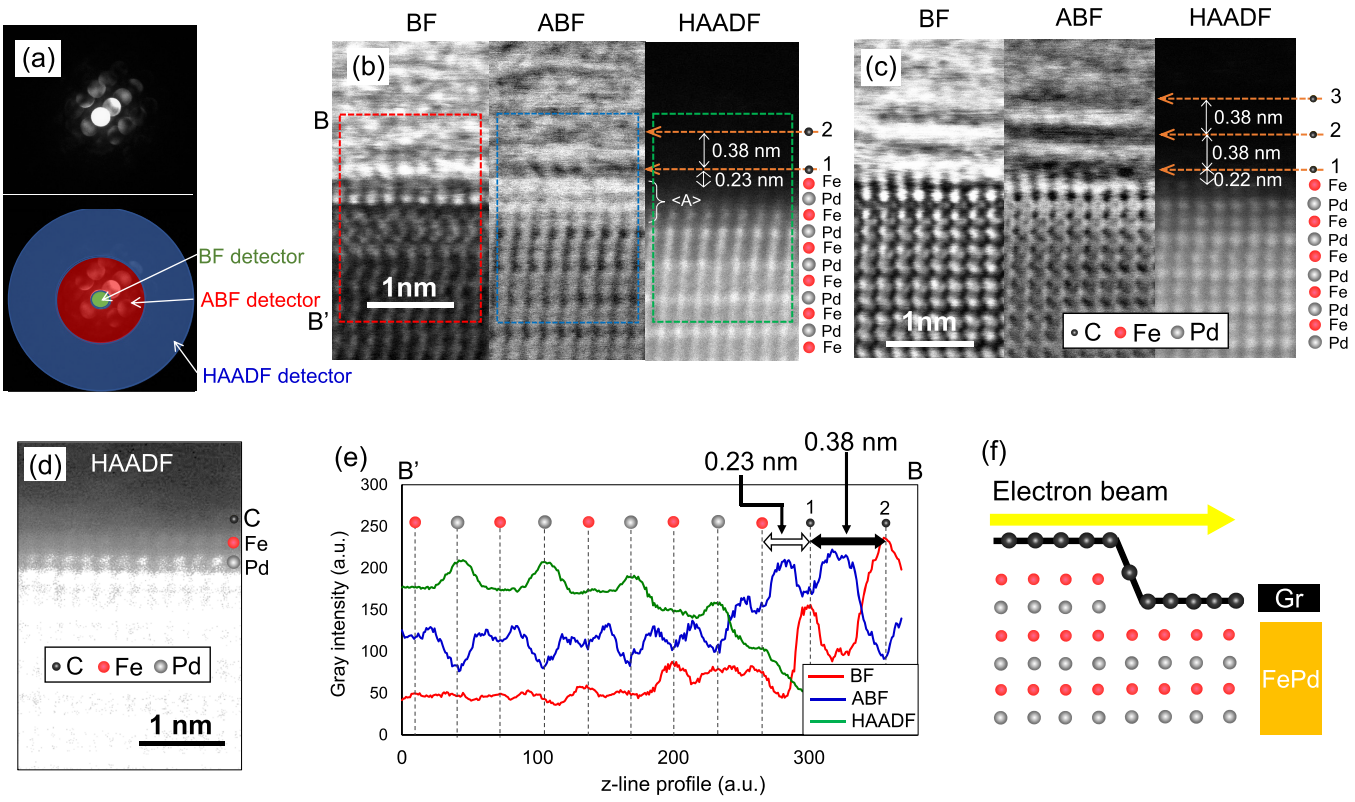

Figure 4. Cross-sectional scanning tunnel electron microscopy (STEM) observations using three different detectors: bright-field (BF), annular bright-field (ABF), and high-angle annular dark-field (HAADF). The incidence of the electron beam is $[110]_{L1_0}$. (a) Acceptance angles for BF, ABF, and HAADF were 0−10.1, 10.1−79.5, and 79.5−200 mrad, respectively. STEM observation for (b) single or bilayer graphene and (c) trilayer graphene. (d) Visualization of the interface of the FePd-side HAADF-STEM image by contrast adjustment. The outermost surface atom of FePd was identified primarily as Fe rather than Pd. (e) *z*-line profiles of the out-of-plane direction obtained from STEM images in (b). *z*-line profile averaged from the *x*-direction in the dashed square area. (f) Schematic illustration of electron beam incident direction to the step−terrace interface formed at the Gr/FePd layer.

first layer of Gr was approximately 0.23 nm. The interatomic distance in the out-of-plane direction of the FePd unit cell was approximately 0.38 nm in the HAADF-STEM images. The out-of-plane distances estimated from the STEM images are listed in Table 2. The bright contrast ⟨*A*⟩ at FePd in the ABF-STEM image is attributed to the strain from Gr and/or overlapping of heavy and light atoms due to the thickness of the STEM samples (Figure 4f). Figure 4c shows another region of the STEM sample. It was confirmed that this region contained three Gr layers on the FePd layer, and the interatomic distance between the Fe in FePd and carbon of Gr was 0.22 nm, which is consistent with the observation in Figure 4b. The interatomic distance between the second and third Gr layers was approximately 0.38 nm, which was larger than that of the interatomic distance between first Gr layer and Fe layer in FePd.

To understand the experimentally observed STEM images, the atomic positions and interatomic distances at the Gr/FePd interface were computationally predicted using first-principles calculations. First-principles structural optimization using the VASP code with PBE[39] for exchange−correlation was performed, and Grimme's DFT-D2 method[40] for the vdW interaction was used. The HAADF-STEM image (Figure 4d) reveals that the outermost surface atom of FePd was primarily Fe. Then, the possible supercells of Fe atoms, covered periodically by hexagonal Gr, were investigated. The calculations were performed using three layers of FePd and mono- and bilayer Gr. During the calculation, the atomic positions of the lower end of the three layers of FePd were fixed, and those at upper FePd and Gr layers were relaxed. The energy at each atomic position was calculated by rotating tetragonal $L1_0$-FePd

Table 2. Interatomic Distance to the Out-of-Plane Direction Deduced from Scanning Tunnel Electron Microscopy (STEM) Images of Bilayer and Trilayer Gr in Figure 4b and c, Respectively[a]

Fig. 4b	Gr	FePd
Gr layer	0.38 nm	
Gr/FePd Interface	**0.23 nm**	0.39 nm
FePd inner layer	-	0.38 nm

Fig. 4c	Gr	FePd
Gr layer	0.38 nm	
Gr/FePd Interface	**0.22 nm**	0.38 nm
FePd inner layer	0.39 nm	0.38 nm

[a]The interatomic distance of Gr and FePd layers was approximately 0.2 nm. The shorter interatomic distance compared with graphite (0.355 nm) indicates that the chemisorption-type van der Waals (vdW) force was bonded Gr and FePd. The lattice distance to the perpendicular direction of FePd is almost constant (approximately 0.38 nm).

https://doi.org/10.1021/acsnano.1c09843
ACS Nano 2022, 16, 4139−4151

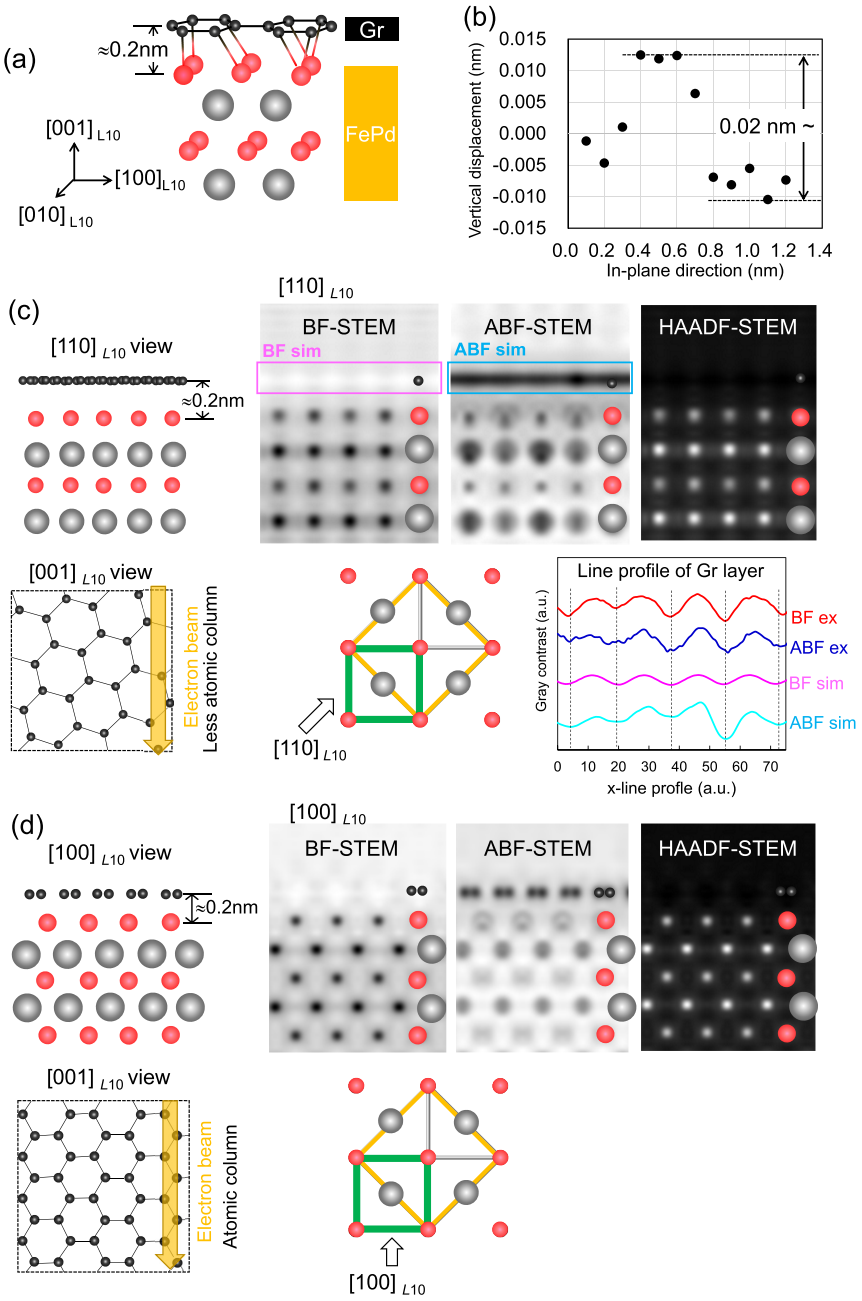

Figure 5. Atomic positions calculated *via* first-principles calculation based on van der Waals (vdW) force. (a) Stable structure of a crystallographically heterogeneous Gr/FePd interface of the 3D image. The armchair axis of Gr is parallel to the FePd $[100]_{L10}$. (b) Calculated vertical displacement *versus* in-plane direction for the first layer of Gr taking into consideration the many coordinations of Fe and C atoms at the interface. (c) Simulated BF, ABF, and HAADF-STEM images from electron beam incident $[110]_{L10}$. The atomic model of the cross-sectional image $[110]_{L10}$ view of Gr/FePd and in-plane image $[001]_{L10}$ view for only carbon atoms. In the $[001]_{L10}$ view, the carbon atoms had less of an atomic column arrangement with respect to the incident electron beam. The line profiles to the in-plane direction of the Gr layer are shown. The line profiles were estimated from BF and ABF-STEM images in the experiment (4b), which is described as BF_{ex} (red line) and ABF_{ex} (blue line), respectively. The line profiles deduced from simulated BF and ABF-STEM images are described as BF_{sim} (pink line) and ABF_{sim} (light blue line), respectively. The crystal structure of face-centered cubic (fcc) and $L1_0$-ordered FePd alloy and relation to the incident direction of the electron beam are indicated. Here, the $L1_0$-ordered structure was used and described as $[100]_{L10}$ and $[110]_{L10}$. (d) Simulation of STEM images from $[100]_{L10}$. The two pairs of atomic columns were confirmed from electron beam incident $[100]_{L10}$.

toward hexagonal Gr. Consequently, an energetically stable atomic configuration of the crystallographically heterogeneous Gr/$L1_0$-FePd interface was proposed. A schematic illustration of the three-dimensional view of the atomic positions is shown in Figure 5a. The atomic relationship between carbon and Fe has been determined theoretically. The Gr armchair axis is parallel to FePd $[100]_{L10}$, where Gr has a small strain by influence of chemical bonding.[37] The interatomic distance in the first layer of Gr and the Fe layer of FePd was determined to be approximately 0.2 nm, which is consistent with the experimentally observed interatomic distances in the BF- and ABF-STEM images (Figure 4b and c). The interatomic distance in the first and second Gr upper layers becomes larger (≈0.32 nm), which roughly agrees with the experimentally confirmed interatomic distance of 0.38

https://doi.org/10.1021/acsnano.1c09843
ACS Nano 2022, 16, 4139−4151

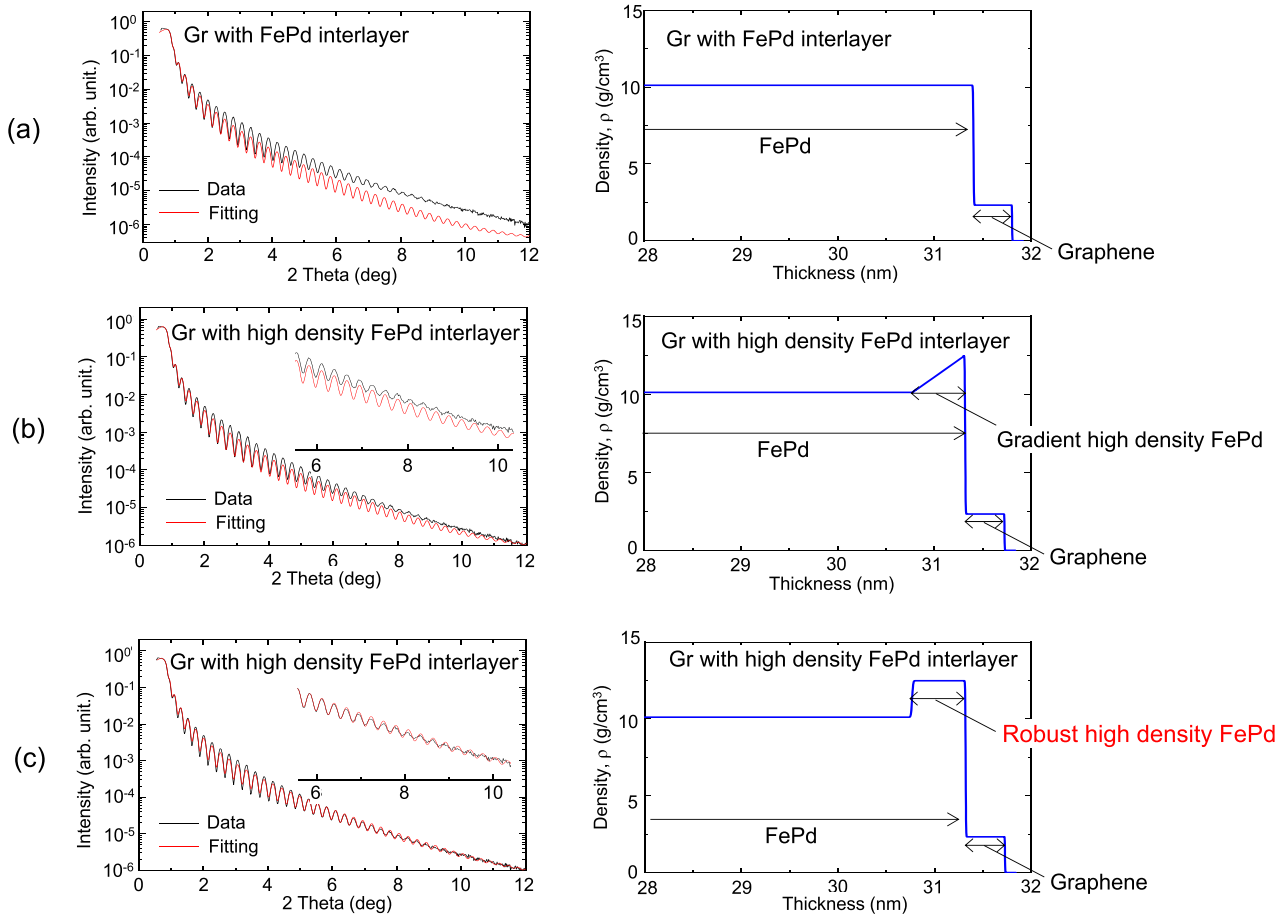

Figure 6. X-ray reflectivity (XRR) measurement of Gr/FePd and three typical fitting results for describing different interfacial structures: (a) continuous mass density, (b) higher mass density gradient, (c) robust high mass density at the FePd side of the interface. The mass density in the vertical axis is proportional to the electron density in XRR fitting equation. At 2 theta above 6 degrees, the XRR data are strongly related to the Gr layer. Fitting in (c) matched well with the experimental data in the whole angle.

nm (Figure 4b and c). The interatomic distance in the Gr/FePd layer was shorter than that in the upper Gr layers. The interatomic distance in the Gr upper layers (≈0.32 nm) is close to that in graphite (0.355 nm),[41] which indicates that the upper Gr layers have physisorption-type vdW forces. In the case of 3-fold symmetric crystal interfaces such as *h*-BN or Gr/Co,[12,13] the interatomic distance was short, and a chemisorption-type vdW force with strong orbital hybridization was observed. Therefore, shortening the interatomic distance at the Gr/FePd interface resulted in a chemisorption-type vdW force with strong orbital hybridization. Figure 5b shows the calculated local vertical displacement of each carbon at the first Gr layer as a function of the in-plane direction. The average displacement of the vertical direction was set to zero (Figure 5b). The maximum displacement in the vertical direction was approximately 0.02 nm. There are many carbons coordinated with respect to Fe atoms in $L1_0$-FePd owing to the crystallographically heterogeneous interface, and the strength of the orbital hybridization is dependent on the bonding length. Note that vertical displacement is observed only in the first layer of Gr and almost no influence on the upper second layer of Gr. The influence of FePd on the upper Gr layers is low, and as a result, orbital hybridization weakens. The influence of orbital hybridization from FePd is localized to an extremely short distance, which is evidence of robustness. In the calculation, it was indicated that shortening the interatomic distance induces robust orbital hybridization only at the interface between FePd and first layer of Gr, which is consistent with the experimental XMCD and STEM results.

To determine the atomic position, the experimentally observed STEM images were reproduced by simulation using Win HREM software (HREM Research).[42] The atomic coordination deduced from first-principles calculation was used for the STEM image simulation. The STEM simulation was carried out from the electron beam incident on $[110]_{L10}$ (Figure 5c) and $[100]_{L10}$ (Figure 5d). The unit cells of $L1_0$ and face-centered cubic (fcc) are denoted by the green and orange squares, respectively. From the $[110]_{L10}$ view (Figure 5c), the first Gr layer in the BF- and ABF-STEM simulated images would be seen as connected contrast among dots. This continuous contrast is roughly consistent with the experimentally observed BF- and ABF-STEM images. The continuity of the Gr layer from the $[110]_{L10}$ view can be explained by the lower atomic column arrangement against the incident electron beam. The line profile for the in-plane direction was obtained around the first Gr layer in both simulated STEM images and experimentally observed STEM images. The in-plane line profiles from the BF- and ABF-SETM image simulations are denoted BF_{sim} and ABF_{sim}, respectively (Figure 5c). The pink and light blue squares respectively indicate the area of the line profiles for BF_{sim} and ABF_{sim}. The in-plane line profiles deduced from the experimentally observed BF- and ABF-STEM images in Figure

https://doi.org/10.1021/acsnano.1c09843
ACS Nano 2022, 16, 4139−4151

4b are denoted BF_{ex} and ABF_{ex}, respectively. Line profiles of BF_{ex} and ABF_{ex} were obtained from the first Gr layer. The gray contrast of the in-plane line profiles corresponds to the sum of the overlapping carbon atoms. For example, when the gray contrast was small, a small number of carbon atoms were aligned in the direction of the electron beam. The line profiles are related to the extent to which the carbon atoms were overlapped; therefore, the line profiles can be used to ensure consistency in structural similarity. The periodicity of gray contrast of in-plane line profiles of carbon in BF_{ex}, ABF_{ex}, BF_{sim}, and ABF_{sim} was the same. This consistency indicates that the theoretical prediction is in good agreement with the experimentally observed STEM results. Thus, from the interfacial atomic position of Gr grown by CVD on the epitaxial $L1_0$-FePd, it is confirmed theoretically and experimentally that the armchair axis of Gr is parallel to that of FePd $[100]_{L10}$. Hence, it was confirmed that the crystal orientation of hexagonal Gr toward the tetragonal $L1_0$-FePd selects an energetically stable structure based on the vdW force. Figure 5d shows STEM simulation images of the electron beam incident from $[100]_{L10}$. In $[100]_{L10}$, the carbon forms an atomic column with respect to the electron beam direction, and thus, two pairs of contrasts were simulated in the BF- and ABF-STEM images. The atomic position in the in-plane direction can be determined from a clearer image from the $[100]_{L10}$ incident.

STEM observations reveal the details of the interfacial structure in the local area. The wider areas of the surface and interface were confirmed by atomic force microscopy (AFM), optical microscopy, Raman spectroscopy, and X-ray reflectivity (XRR) analysis. The evaluation of surface morphology by AFM, optical microscopy, and Raman observations was described in the Supporting Information. Here, the content of surface characteristics was briefly explained. AFM was used to evaluate the surface morphology of the $L1_0$-FePd film without Gr. The $L1_0$-FePd surface was atomically flat, and the average roughness was below 0.4 nm (see the Supporting Information) To evaluate the quality of the Gr layer on the $L1_0$-FePd, optical microscopy and Raman spectroscopy observations were carried out (see the Supporting Information). The optical microscopy indicated that the Gr layer showed homogeneous contrast, and a pinhole-like defect was not observed. Raman spectroscopy using the G peak signature showed a homogeneous contrast, indicating that the Gr on $L1_0$-FePd was homogeneously covered in a wide area. To evaluate the average number of Gr layers and the density at the Gr/$L1_0$-FePd interface, XRR measurements were performed (Figure 6). The XRR can be used to estimate the thickness, roughness, and density of each layer. Not all parameters can be obtained by fitting. Some fixed parameters used for the fitting are required in advance to perform an XRR fitting with accuracy. The thickness of the FePd layer was approximately 31 nm, as measured from cross-sectional HAADF-STEM images. The density of the FePd inner layer was calculated using HAADF-STEM images, which is almost the same as the bulk value. AFM and microscopy observations confirmed that the FePd and Gr layers were flat. These parameters can then be used as fixed values. Thereby, the density at the interface and thickness of the Gr layer were chosen as primary fitting parameters. XRR was measured from 0.5° to 10° in the 2-theta. An angle of more than 6° is caused by graphene, so the fitting was performed by emphasizing the high-angle side. Using the criteria mentioned above, three typical interfacial structures focusing on the interface are presented in Figure 6: (i) the FePd has a continuous density in the vertical direction (Figure 6a); (ii) a gradient high density at the interface (Figure 6b); (iii) a constant robust high density at the interface (Figure 6c). The constant density (Figure 6a) indicates that the fitting curve is under the experimental XRR data. The high-density gradient at the interface (Figure 6b) approached the experimental XRR data. However, beyond 6°, the high-density gradient was slightly mismatched (inset of Figure 6b). As mentioned above, the XRR at a higher angle exceeding 6° was affected by Gr, because Gr is a lightweight element, which causes a density contrast against FePd. Better fitting in whole angle was realized by the constant robust high density at the interface (Figure 6c). The layer information used in the fitting, as shown in Figure 6c, is summarized in Table 3. The thickness of Gr was investigated by changing monolayer to trilayer with fixing the fitting parameters. As a result, the average thickness of the Gr layer was 0.4 nm (Table 3). In other words, Gr was approximately bilayered. This means that the average picture of our sample is described in Figure 4b, which shows the bilayer Gr. In this section, we are going to discuss the meaning of density in XRR. According to the STEM observations (Figures 4b and c), the mass density at the interface of FePd is not high. This was because there was almost no change in the lattice spacing in the out-of-plane and in-plane directions. The density (ρ) can be expressed as

$$\rho = \frac{\rho_0 A}{\lambda N_A (Z + f' + if'')} \tag{2}$$

where ρ_0, A, λ, N_A, Z, and $f' + if''$ are the electron density, atomic weight, wavelength, Avogadro's number, atomic number, and anomalous scattering factor of the atomic scattering factor, respectively. In eq 2, ρ is proportional to the electron density (ρ_0). Therefore, it can be considered that the shortening of the interatomic distance in FePd and the first Gr layers increases ρ_0 at the interface. The robustness of ρ_0 at the interface (Figure 6c) coincides with that of robust M_l at the interface, which was determined by depth-resolved XMCD analyses (Figure 3b). From these multifaceted analyses, it was revealed that shortening of the interatomic distance produces a robust high ρ_0 and chemisorption-type vdW force and that eventually the robust interfacial anisotropic M_l emerges as a consequence of strong orbital hybridization at the Gr/$L1_0$-FePd interface.

Table 3. Thickness, Roughness, and Mass Density (ρ) of Each Layer Deduced by X-ray Reflectivity (XRR) Fitting for the Interfacial Layer with High Robust Mass Density (Figure 6(c))[a]

Fig. 6(c)	Thickness (nm)	Roughness (nm)	Density (g/cm^3)
C	0.4	0.002	2.327
FePd interlayer	0.6	0.004	12.488
FePd	30.8	0.009	10.115
$SrTiO_3$ sub.	-	0.278	5.117

[a]In the XRR measurement, the ρ of the fitting parameter is proportional to electron density (ρ_0). $\rho = \frac{\rho_0 A}{\lambda N_A (Z + f' + if'')}$, where ρ_0, A, λ, N_A, Z, and $f' + if''$ are electron density, atomic weight, wavelength, Avogadro's number, atomic number, and anomalous scattering factor of the atomic scattering factor.

Discussion on Gr/$L1_0$-FePd Hybrid MTJs for X nm Generation MRAM. $L1_0$-FePd has the advantage of data

https://doi.org/10.1021/acsnano.1c09843
ACS Nano 2022, 16, 4139−4151

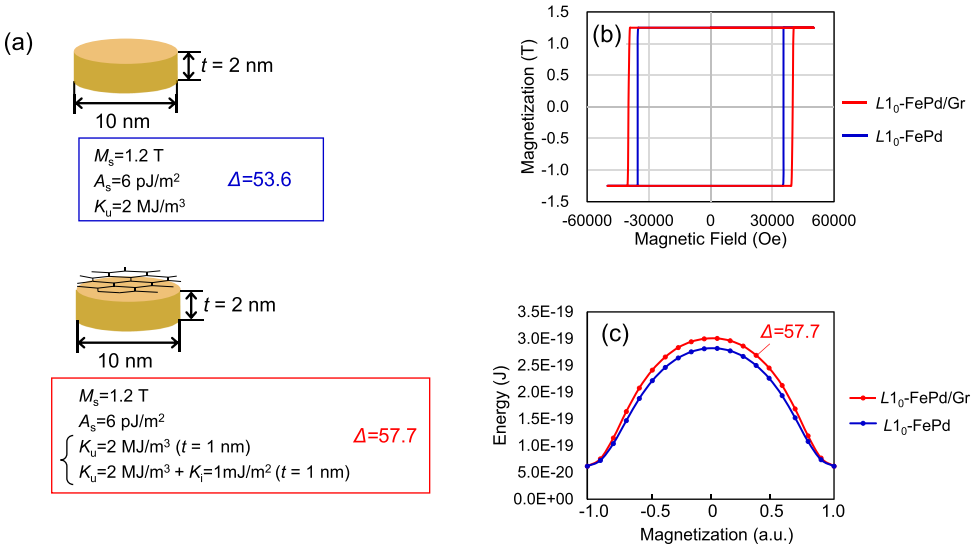

Figure 7. Micromagnetic simulation assuming a small FePd recording layer (thickness = 2 nm; circular diameter = 10 nm) (a) without Gr and with Gr. Calculation was performed using the string method. (b) The magnetization curves by applying magnetic field to perpendicular direction. (c) The thermal stability factor Δ exceeding 57 implies that an information retention period of more than 10 years can be obtained.

retention in high-density p-MTJs owing to its high uniaxial MAE. In our previous study,[25] $L1_0$-FePd combined with MgO tunnel barriers required 001 epitaxial growth for Δ_1 coherent tunneling. However, the MgO/$L1_0$-FePd interface deteriorated due to a large epitaxial lattice mismatch of approximately 10%, which decreased the TMR ratio because of the reduced efficiency of Δ_1 coherent tunneling. Consequently, p-MTJs with $L1_0$-FePd and a MgO barrier required insertion layers between $L1_0$-FePd and MgO to reduce the lattice misfit in a step-by-step manner for the TMR ratio.[25] However, the step-by-step technique was limited by large lattice misfit between the $L1_0$-FePd and MgO layers. In contrast, our research revealed that, owing to the highly flexible bonding of the vdW force, a flat interface could be formed. Thus, the TMR ratio will not be degraded by the rough interface in the p-MTJs consisting of an $L1_0$-FePd recording layer and a Gr tunneling barrier. Focusing on the relationship between scaling and microfabrication damage, the smaller recording layer increases the volume ratio of damage caused by the formation of an oxidation layer during the microfabrication process. The proportion of the damaged layer becomes significant in the X-nm-generation MRAM, where X nm is the diameter of the recording layer. A damaged layer during the microfabrication process is formed on the sidewall at a thickness of approximately 5 nm in the case of CoFeB/MgO p-MTJs.[43] The 3*d* transition metals of Co and Fe have weak oxidation resistance. Conversely, precious metal ordered alloys such as $L1_0$-FePd have better oxidation resistance; therefore, precious metals are preferable for reducing sidewall damage. Consequently, it can be considered that the combination of $L1_0$-FePd as a recording layer and Gr as a tunneling barrier has an advantage in the X nm generation from the viewpoint of sidewall as well as interfacial damage. As mentioned above, IPMA appears at the FePd/Gr interface. Then, the total PMA is the summation of not only the high bulk PMA of $L1_0$-FePd but also the IPMA. To clarify the usefulness of IPMA with the Gr/FePd interface combined with large bulk PMA using $L1_0$-FePd, a micromagnetic simulation was performed using a small recording layer. In the Gr/$L1_0$-FePd p-MTJ, the FePd recording layer had a circular diameter of 10 nm and a thickness of 2 nm. The size of the recording layer was on the border of the X nm generation. A saturation magnetization of 1.2 T, exchange stiffness constant of 6 pJ/m^2, and bulk PMA value of 2 MJ/m^3 were used for calculation; these parameters were magnetic properties at RT.[44] The IPMA value was set to be 1 mJ/m^2.[14] The influence of IPMA was set to 1 nm with robustness. The coercive field and thermal stability (Δ) increased by approximately 8% owing to the addition of the IPMA (Figure 7a). The size on the border of the X nm generation demonstrated that the bulk PMA of $L1_0$-FePd contributed to the total PMA more than that of the IPMA. It can be considered that the effect of IPMA becomes more apparent when the size is thinner in the X nm generation. The Δ exceeded 57 in the Gr/FePd small dot (Figure 7b), which means that the data retention is more than 10 years. Such high data retention characteristics are difficult to realize by simply using CoFeB/MgO p-MTJs.[17,18] In such a small recording layer, not only IPMA of CoFeB/MgO but also the shape magnetic anisotropy (SMA)[43] are necessary. In the case of the CoFeB/MgO p-MTJ with IPMA and SMA, optimization of the combination ratio of IPMA and SMA is necessary to reduce the total volume of the magnetic layer for reduction of the switching current. In addition, it is necessary to establish a highly damage-controlled microfabrication process for the CoFeB/MgO hybrid p-MTJs. We believe that there are many breakthrough technologies for realizing the X nm generation, such as the combination of IPMA and SMA in CoFeB/MgO p-MTJs and Gr/$L1_0$-FePd hybrid p-MTJs, and each method is a candidate for bridging the technological progress. The micromagnetic simulation of the Gr/$L1_0$-FePd p-MTJ proposed that the flexible bond of the vdW force increased the degree of freedom at the interface and is highly valuable for practical use. We think that large bulk PMA combined with IPMA using Gr/$L1_0$-FePd p-MTJs is one of the candidate technologies for high-density X-nm-generation MRAM.

CONCLUSIONS

Robust anisotropic interfacial M_l emerged at the crystallographically heterogeneous Gr (averagely bilayer)/$L1_0$-FePd (31 nm) bilayer. The interatomic distance between the Gr and FePd

https://doi.org/10.1021/acsnano.1c09843
ACS Nano 2022, 16, 4139−4151

layers was confirmed theoretically and experimentally as approximately 0.2 nm, which is shorter than the range of the physisorption-type vdW force (0.355 nm in graphite). This shortening of the interatomic distance is due to chemisorption-type vdW force. The short interatomic distance increases the electron density, resulting in strong orbital hybridization, and, eventually, a robust interfacial M_I emerges at the interface. The in-plane crystal orientation of the Gr formed by CVD, which cannot be artificially determined by, for example, the peeling method, was determined theoretically and experimentally as follows: the Gr armchair axis is aligned parallel to the FePd $[100]_{L10}$, which is an energetically stable interfacial atomic position. Surprisingly, despite the chemisorption-type vdW force, the Gr tolerated its honeycomb structure. The high degree of $L1_0$-ordering maintained until the surface of the $L1_0$-FePd layer, which faces Gr, is an advantage over $L1_0$-FePd/MgO-type MTJs. By micromagnetic simulation, the robust IPMA of the Gr/FePd interface in cooperation with the large PMA of the $L1_0$-FePd has the potential to demonstrate data retention over 10 years in ultrasmall p-MTJs, which can be targeted for X-nm-generation MRAM devices. Our concept in this study is extensible to not only graphene but also many hexagonal 2D-based materials, which are advanced technological building blocks that can combine different materials with a high degree of freedom at crystallographically heterogeneous interfaces.

METHODS

Gr was formed *via* CVD, and $L1_0$-FePd was grown *via* r.f. magnetron sputtering (EIKO Co. Ltd.; EW-100NH). The details of the preparation method and concept of the crystallographically heterogeneous interface are described in ref 28. The FePd layer was deposited onto 10 × 10 mm $SrTiO_3$ (001) substrates at RT using a $Fe_{40}Pd_{60}$ atomic percent (at. %) sintered target (76 mm$^{\varphi}$). The composition of the target was adjusted to 40:60 at. % to obtain a 50:50 at. % film composition. The nominal thickness of the FePd film was approximately 30 nm, and the experimentally observed thickness was 31 nm. The FePd films were annealed at 700 °C for 90 min under vacuum using an infrared heater system and cooled to RT. The background pressure prior to the deposition was 2 × 10 $^{-6}$ Pa. Once exposed to the atmosphere, the samples were transferred to a CVD chamber. The FePd films were heated to 600 °C in a 100 Pa H_2 atmosphere at a rate of 300 °C/min and annealed for 15 min to remove the surface oxidation layer. After H_2 was removed and the samples were exposed to a 1 Pa C_2H_2 atmosphere at 600 °C for 15 min, the Gr was formed on the FePd layer.

The experimental setup of depth-resolved XAS and XMCD is illustrated in Figure 8. The XAS and XMCD of the Fe $L_{2,3}$-edges were measured to characterize the Fe states in the FePd layer. The carbon in the Gr layer and Pd in the FePd layer were not measured because of the limitation of the energy region of circularly polarized X-rays at beamline BL-16A. The fluorescence X-rays emitted after XAS were acquired separately at different detection angles (θ_d) using a 1-megapixel soft X-ray charge-coupled device (BK-501X, BITRAN Corp.). The wavelength (λ) was estimated from the attenuation length (l) and detection angle using the following relation: $\lambda = l \sin \theta_d$.[45] The lowest θ_d was determined to be ∼0.1°. By analyzing a set of X-ray data recorded at different wavelengths, depth-resolved XAS and XMCD spectra can be obtained. To analyze the magnetic anisotropy, the magnetic field was tilted by θ_i rotations. θ_is of 90° and 30° mean that a magnetic field of 0.87 T was applied at 90° and 30° from the in-plane direction, respectively. All experiments were performed in a high-vacuum chamber with a base pressure of 1 × 10^{-7} Pa at beamline BL-16A in a photon factory.[46] STEM observations were performed using a Thermo Fisher Scientific Titan G2 60-300 Cubed Themis equipped with a Cs corrector for the STEM probe. Epoxy resin was coated on the Gr/FePd/STO and solidified by baking at 100 °C for 30 min in air. After the epoxy resin solidified, a sample for STEM observation was prepared using a focused ion beam (Thermo Fisher Scientific Versa 3D dual beam system). The probe convergence angle, spherical aberration

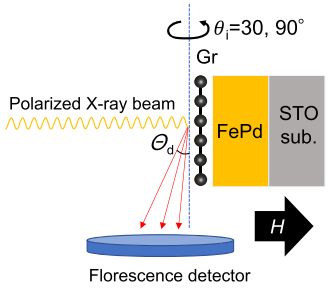

Figure 8. Experimental setup for fluorescence-yield depth-resolved X-ray absorption (XAS) and X-ray magnetic circular dichroism (XMCD). Fluorescence X-ray emitted after XAS was acquired separately at different detection angles θ_d with a charge-coupled device. Lowest θ_d was determined to be ∼0.1°. Magnetic field was tilted by rotations θ_i and θ_is of 90° and 30°, respectively, implying that magnetic field of 0.87 T was applied in the out-of-plane direction and rotated 30° from the in-plane direction.

coefficient (Cs), and accelerating voltage were set to 25 mrad, 0 mm, and 300 kV, respectively. The inner and outer angles for the ABF and HAADF detectors were 10.1 and 79.5 mrad and 79.5 and 200 mrad, respectively. These STEM images were computationally reproduced using Win HREM software.[41] The atomic positions calculated using first-principles calculations were used for the STEM simulation. The simulated STEM images were compared with the experimentally observed STEM images, and the interfacial atomic positions were determined both experimentally and theoretically. The average Gr thickness and electron density at the interface were investigated by XRR measurements using an X-ray diffractometer (D8 Discover Plus, Bruker AXS GmbH). Line-focused X-rays, which were generated by a 5.4 kW rotating anode generator with a 0.3 mm × 3.0 mm filament, were converged and monochromated using a Göbel multilayer mirror. The mirror reduced the angular spreads to $\delta\theta < 2.8 \times 10^{-2}$° for the incidence angle direction of Cu Kα radiation, and the axial divergence was suppressed using Soller slits with angles of 4.0° on both the primary and secondary sides. The incident X-ray beam was formed by the slits and measured 0.05 mm wide and 8.0 mm long. The sample was mounted on an open cradle, and the reflected X-rays were acquired using a multimode detector (EIGER2 R 500 K, DECTRIS AG) after passing through a 0.1-mm-wide antiscattering slit. This multimode detector encompasses an area measuring 77.1 mm × 38.4 mm and controls the active area, similar to the slits. In this experiment, the active area was set to be 0.075 mm wide and 20 mm long. The XRR profile obtained was evaluated *via* simulation fitting using the DIFFRAC.LEPTOS software package (Bruker AXS GmbH). To demonstrate the practical usefulness of Gr/FePd p-MTJs, the magnetic hysteresis ($M - H$) loops, energy barrier (E), and thermal stability (Δ) were calculated *via* micromagnetic simulation,[47,48] *via* the string method.[49,50] The string method is effective in identifying the minimum energy path between the parallel (P) and antiparallel (AP) states of MTJs. Δ was calculated by taking into consideration the magnetic energy states of the demagnetization energy, E_d, anisotropy energy, E_{ani}, exchange energy, E_{exc}, and total energy, E_{all}, for the z-axis (out-of-plane direction). These energy parameters are calculated in 20 points in the free energy landscape between AP, P, and bistable states.

ASSOCIATED CONTENT

Supporting Information

The Supporting Information is available free of charge at https://pubs.acs.org/doi/10.1021/acsnano.1c09843.

Surface morphology and quality of Gr/$L1_0$-FePd evaluated by AFM (Figure 1S); optical microscopy and Raman spectroscopy observations (Figure 2S) (PDF)

https://doi.org/10.1021/acsnano.1c09843
ACS Nano 2022, 16, 4139−4151

AUTHOR INFORMATION

Corresponding Author

Hiroshi Naganuma − *Center for Spintronics Integrated Systems (CSIS), Tohoku University, Sendai, Miyagi 980-8577, Japan; Center for Innovative Integrated Electronics Systems (CIES), Tohoku University, Sendai, Miyagi 980-8572, Japan; Center for Spintronics Research Network (CSRN), Tohoku University, Sendai, Miyagi 980-8577, Japan; Graduate School of Engineering, Tohoku University, Sendai, Miyagi 980-8579, Japan;* orcid.org/0000-0003-2966-8269; Email: hiroshi.naganuma.c3@tohoku.ac.jp

Authors

Masahiko Nishijima − *The Electron Microscopy Center, Tohoku University, Sendai, Miyagi 980-8577, Japan*

Hayato Adachi − *Graduate School of Engineering, Kobe University, Kobe, Hyogo 657-8501, Japan*

Mitsuharu Uemoto − *Graduate School of Engineering, Kobe University, Kobe, Hyogo 657-8501, Japan*

Hikari Shinya − *Research Institute of Electrical Communication, Tohoku University, Sendai, Miyagi 980-8577, Japan; Center for Spintronics Research Network (CSRN), Graduate School of Engineering Science, Osaka University, Toyonaka, Osaka 560-8531, Japan*

Shintaro Yasui − *Laboratory for Materials and Structures, Institute of Innovative Research, Tokyo Institute of Technology, Meguro-ku, Tokyo 152-8550, Japan; Laboratory for Zero-Carbon Energy, Tokyo Institute of Technology, Meguro-ku, Tokyo 152-8550, Japan;* orcid.org/0000-0003-0524-9318

Hitoshi Morioka − *Application Laboratory, Application Department, X-ray Division, Bruker Japan K. K., Yokohama, Kanagawa 221-0022, Japan*

Akihiko Hirata − *School of Fundamental Science and Engineering, Faculty of Science and Engineering, Waseda University, Shinjuku-ku, Tokyo 169-8555, Japan*

Florian Godel − *Unité Mixte de Physique, CNRS/Thales, 91767 Palaiseau, France; Université Paris-Saclay, 91767 Palaiseau, France;* orcid.org/0000-0003-1741-2741

Marie-Blandine Martin − *Unité Mixte de Physique, CNRS/Thales, 91767 Palaiseau, France*

Bruno Dlubak − *Center for Spintronics Integrated Systems (CSIS), Tohoku University, Sendai, Miyagi 980-8577, Japan; Unité Mixte de Physique, CNRS/Thales, 91767 Palaiseau, France;* orcid.org/0000-0001-5696-8991

Pierre Seneor − *Center for Spintronics Integrated Systems (CSIS), Tohoku University, Sendai, Miyagi 980-8577, Japan; Unité Mixte de Physique, CNRS/Thales, 91767 Palaiseau, France; Université Paris-Saclay, 91767 Palaiseau, France*

Kenta Amemiya − *Institute of Materials Structure Science, High Energy Accelerator Research Organization, Tsukuba, Ibaraki 305-0801, Japan; Department of Materials Structure Science, The Graduate University for Advanced Studies (SOKENDAI), Tsukuba, Ibaraki 305-0801, Japan; Department of Chemistry, School of Science, The University of Tokyo, Bunkyo-ku, Tokyo 113-8656, Japan;* orcid.org/0000-0003-2415-6686

Complete contact information is available at: https://pubs.acs.org/10.1021/acsnano.1c09843

Author Contributions

H.N. conceived this work, designed the interfacial specific analytical experiments, and wrote the first draft. The concept of a crystallographically heterogeneous bilayer structure was proposed by H.N., B.D., and P.S. H.N. grew the $L1_0$-FePd, and F.G., M-B.M., B.D., and P.S. fabricated the Gr that was reported previously. The main topic of this work was interfacial analysis, which was assigned as follows. K.A. and H.N. measured and analyzed XMCD and found IPMA. M.N. and H.N. observed cross-sectional STEM, and A.H. simulated the STEM images. H.A., M.U., and H.S. carried out theoretical analysis at interfacial structures by first-principal calculations. S.Y., H.N., and H.M. measured and analyzed XRR. All authors contributed to the discussion of the results and the preparation of the final version of the manuscript.

Notes

The authors declare no competing financial interest.

ACKNOWLEDGMENTS

This study was partly supported by Center for Spintronics Integrated Systems (CSIS) in Tohoku University, Japan Society for the Promotion of Science (JSPS) Core-to-Core Program (No. JPJSCCA20160005), and cross-appointment project in CSIS Tohoku University. This work has been performed under the approval of the Photon Factory Program Advisory Committee (K.A.) (No. 2019S2-003), nanotechnology platform in Tohoku University (H.N. and M.N.) (No. A-20-TU-0063), and collaborative Research Project of Laboratory for Materials and Structures, Institute of Innovative Research, Tokyo Institute of Technology (S.Y. and H.N.) (No. 76). H.N. thanks Dr. In-T. Bae, University of New York in Binghamton, and Prof Shiraishi, Tokyo Institute of Technology, for fruitful discussions about STEM. H.N. thanks Prof. T. Ono, Kobe University for discussion about theoretical calculation.

REFERENCES

(1) Bhimanapati, G. R.; Lin, Z.; Meunier, V.; Jung, Y.; Cha, J.; Das, S.; Xiao, D.; Son, Y.; Strano, S.; Cooper, V. R.; Liang, L.; Louie, S. G.; Ringe, E.; Zhou, W.; Kim, S. S.; Naik, R. R.; Sumpter, B. G.; Terrones, H.; Xia, F.; Wang, Y.; et al. Recent Advances in Two-Dimensional Materials beyond Graphene. *ACS Nano* **2015**, *9*, 11509−11539.

(2) Tombros, N.; Jozsa, C.; Popinciuc, M.; Jonkman, H. T.; Wees, B. J. v. Electronic spin transport and spin precession in single graphene layers at room temperature. *Nature* **2007**, *448*, 571−574.

(3) Cho, S.; Chen, Y.-Fu.; Fuhrer, M. S. Gate-tunable graphene spin valve. *Appl. Phys. Lett.* **2007**, *91*, 123105.

(4) Sichau, J.; Prada, M.; Anlauf, T.; Lyon, T. J.; Bosnjak, B.; Tiemann, L.; Blick, R. H. Resonance Microwave Measurements of an Intrinsic Spin-Orbit Coupling Gap in Graphene: A Possible Indication of a Topological State. *Phys. Rev. Lett.* **2019**, *122*, 04603.

(5) Yang, H.; Chen, G.; Cotta, A. A. C.; N'Diaye, A. T.; Nikolaev, S. A.; Soares, E. A.; Macedo, W. A. A.; Liu, K.; Schmid, A. K.; Fert, A.; Chshiev, M. Significant Dzyaloshinskii-Moriya interaction at graphene-ferromagnet interfaces due to the Rashba effect. *Nat. Mater.* **2018**, *17*, 605−609.

(6) Gmitra, M.; Konschuh, S.; Ertler, C.; Ambrosch-Draxl, C.; Fabian, J. Band-structure topologies of graphene: Spin-orbit coupling effects from first principles. *Phys. Rev. B* **2009**, *80*, 235431.

(7) Li, X.; Wu, Z.; Liu, J. Rashba spin-orbit coupling in graphene monolayer coated by periodic magnetic stripes. *Sci. Rep.* **2017**, *7*, 6526.

(8) Gong, S. J.; Li, Z. Y.; Yang, Z. Q.; Gong, C.; Duan, C.-G.; Chu, J. H. Spintronic properties of graphene films grown on Ni(111) substrate. *J. Appl. Phys.* **2011**, *110*, 043704.

(9) Han, W.; Kawakami, R. K.; Gmitra, M.; Fabian, J. Graphene spintronics. *Nat. Nanotechnol.* **2014**, *9*, 794−807.

(10) Karpan, V. M.; Giovannetti, G.; Khomyakov, P. A.; Talanana, M.; Starikov, A. A.; Zwierzycki, M.; van den Brink, J.; Brocks, G.; Kelly, P. J.

Graphite and Graphene as Perfect Spin Filters. *Phys. Rev. Lett.* **2007**, *99*, 176602.
(11) Dlubak, B.; Martin, M.-B.; Weatherup, R. S.; Yang, H.; Deranlot, C.; Blume, R.; Shloegl, R.; Fert, A.; Anane, A.; Hofmann, S.; Seneor, P.; Robertson, J. Graphene-Passivated Nickel as an Oxidation-Resistant Electrode for Spintronics. *ACS Nano* **2012**, *6*, 10930−10934.
(12) Piquemal-Banci, M.; Galceran, R.; Dubois, S. M. -M.; Zatko, V.; Galbiati, M.; Godel, F.; Martin, M.-B.; Weatherup, R. S.; Petroff, F.; Fert, A.; Charlier, J.-C.; Robertson, J.; Hofmann, S.; Dlubak, B.; Seneor, P. Spin filtering by proximity effects at hybridized interfaces in spin-valves with 2D graphene barriers. *Nat. Commun.* **2020**, *11*, 5670.
(13) Lu, H.; Robertson, J.; Naganuma, H. Comparison of hexagonal boron nitride and MgO tunnel barriers in Fe,Co magnetic tunnel junctions. *Appl. Phys. Rev.* **2021**, *8*, 031307.
(14) Yang, H.; Vu, A. D.; Hallal, A.; Rougemaille, N.; Coraux, J.; Chen, G.; Schmid, A. K.; Chshiev, M. Anatomy and Giant Enhancement of the Perpendicular Magnetic Anisotropy of Cobalt-Graphene Heterostructures. *Nano Lett.* **2016**, *16*, 145−151.
(15) Li, W.; Xue, L.; Abruna, H. D.; Ralph, D. C. Magnetic tunnel junctions with single-layer-graphene tunnel barriers. *Phys. Rev. B* **2014**, *89*, 184418.
(16) Ikeda, S.; Miura, K.; Yamamoto, H.; Mizunuma, K.; Gan, H. D.; Endo, M.; Kanai, S.; Hayakawa, J.; Matsukura, F.; Ohno, H. A perpendicular-anisotropy CoFeB-MgO magnetic tunnel junction. *Nat. Mater.* **2010**, *9*, 721−724.
(17) Sato, H.; Enobio, E. C. I.; Yamanouchi, M.; Ikeda, S.; Fukami, S.; Kanai, S.; Matsukura, F.; Ohno, H. Properties of magnetic tunnel junctions with a MgO/CoFeB/Ta/CoFeB/MgO recording structure down to junction diameter of 11 nm. *Appl. Phys. Lett.* **2014**, *105*, 062403.
(18) Naganuma, H.; Miura, S.; Honjo, H.; Nishioka, K.; Watanabe, T.; Nasuno, T.; Inoue, H.; Nguyen, T. V. A.; Endo, Y.; Noguchi, Y.; Yasuhira, M.; Ikeda, S.; Endoh, T. Advanced 18 nm Quad-MTJ technology overcomes dilemma of Retention and Endurance under Scaling beyond 2X nm. *VLSI2021 technical digest* **2021**, T12.
(19) Yang, H. X.; Chishiev, M.; Dieny, B.; Lee, J. H.; Manchon, A.; Shin, K. H. First-principles investigation of the very large perpendicular magnetic anisotropy at Fe|MgO and Co|MgO interfaces. *Phys. Rev. B* **2011**, *84*, 054401.
(20) Parkin, S. S.; Kaiser, C.; Panchula, A.; Rice, P. M.; Hughes, B.; Samant, M.; Yang, S.-H. Giant tunnelling magnetoresistance at room temperature with MgO (100) tunnel barriers. *Nat. Mater.* **2004**, *3*, 862−867.
(21) Yuasa, S.; Nagahama, T.; Fukushima, A.; Suzuki, Y.; Ando, K. Giant room-temperature magnetoresistance in single-crystal Fe/MgO/Fe magnetic tunnel junctions. *Nat. Mater.* **2004**, *3*, 868−871.
(22) Butler, W. H.; Zhang, X.-G.; Schulthess, T. C. Spin-dependent tunneling conductance of Fe|MgO|Fe sandwiches. *Phys. Rev. B* **2001**, *63*, 054416.
(23) Mathon, J.; Umerski, A. Theory of tunneling magnetoresistance of an epitaxial Fe/MgO/Fe(001) junction. *Phys. Rev. B* **2001**, *63*, No. 220403R.
(24) Daalderop, G. H. O.; Kelly, P. J.; Schuurmans, M. F. H. Magnetocrystalline anisotropy and orbital moments in transition-metal compounds. *Phys. Rev. B* **1991**, *44*, 12054−12057.
(25) Naganuma, H.; Kim, G.; Kawada, Y.; Inami, N.; Hatakeyama, K.; Iihama, S.; Islam, K. M. N.; Oogane, M.; Mizukami, S.; Ando, Y. Electrical Detection of Millimeter-Waves by Magnetic Tunnel Junctions Using Perpendicular Magnetized $L1_0$-FePd Free Layer. *Nano Lett.* **2015**, *15*, 623−628.
(26) Mizukami, S.; Wu, F.; Sakuma, A.; Walowski, J.; Watanabe, D.; Kubota, T.; Zhang, X.; Naganuma, H.; Oogane, M.; Ando, Y.; Miyazaki, T. Long-Lived Ultrafast Spin Precession in Manganese Alloys Films with a Large Perpendicular Magnetic Anisotropy. *Phys. Rev. Lett.* **2011**, *106*, 117201.
(27) Slonczewski, J. C. Current-driven excitation of magnetic multilayers. *J. Mag. Mag. Mater.* **1996**, *159*, L1−L7.
(28) Naganuma, H.; Zatko, V.; Galbiati, M.; Godel, F.; Sander, A.; Carretero, C.; Bezencenet, O.; Reyren, N.; Martin, M.-B.; Dlubak, B.; Seneor, P. A perpendicular graphene/ferromagnet electrode for spintronics. *Appl. Phys. Lett.* **2020**, *116*, 173101.
(29) Thole, B. T.; Carra, P.; Sette, F.; van der Laan, G. X-ray circular dichroism as a probe of orbital magnetization. *Phys. Rev. Lett.* **1992**, *68*, 1943−1946.
(30) Carra, P.; Thole, B. T.; Altarelli, M.; Wang, X. X-ray circular dichroism and local magnetic fields. *Phys. Rev. Lett.* **1993**, *70*, 694−697.
(31) Matsumoto, Y.; Entani, S.; Koide, A.; Ohtomo, M.; Avramov, P. V.; Naramoto, H.; Amemiya, K.; Fujikawa, T.; Sakai, S. Spin orientation transition across the single-layer graphene/nickel thin film interface. *J. Mater. Chem. C* **2013**, *1*, 5533−5537.
(32) Dedkov, Yu. S.; Sicot, M.; Fonin, M. X-ray absorption and magnetic circular dichroism of graphene/Ni(111). *J. Appl. Phys.* **2010**, *107*, 09E121.
(33) Weser, M.; Voloshina, E. N.; Horn, K.; Dedkov, Yu. S. Electronic structure and magnetic properties of the graphene/Fe/Ni(111) intercalation-like system. *Phys. Chem. Chem. Phys.* **2011**, *13*, 7534−7539.
(34) Li, W.; Zeng, Y.; Zhao, Z.; Zhang, B.; Xu, J.; Huang, X.; Hou, Y. 2D Magnetic Heterostructures and Their Interface Modulated Magnetism. *ACS Appl. Mater. Interfaces* **2021**, *13*, 50591−50601.
(35) Bruno, P. Tight-binding approach to the orbital magnetic moment and magnetocrystalline anisotropy of transition-metal monolayers. *Phys. Rev. B* **1989**, *39*, 865−868.
(36) Tsujikawa, M.; Hosokawa, A.; Oda, T. Magnetic anisotropy of Fe/Pt(001) and Pt/Fe/Pt(001) using a first-principles approach. *Phys. Rev. B* **2008**, *77*, 054413.
(37) Uemoto, M.; Adachi, H.; Ono, T.; Naganuma, H. Density functional study of atomic and electronic structures of graphene on FePd (001) surface. To be submitted.*to be submitted*
(38) Taniguchi, Y.; Miura, Y.; Abe, K.; Shirai, M. Theoretical Studies on Spin-Dependent Conductance in FePt/MgO/FePt(001) Magnetic Tunnel Junctions. *IEEE Trans. Mag.* **2008**, *44*, 2585−2588.
(39) Perdew, J. P.; Burke, K.; Ernzerhof, M. Generalized Gradient Approximation Made Simple. *Phys. Rev. Lett.* **1996**, *77*, 3865−3868.
(40) Grimme, S. Semiempirical GGA-type density functional constructed with a long-range dispersion correction. *J. Comput. Chem.* **2006**, *27*, 1787−1799.
(41) Ishizuka, K. A practical approach for STEM image simulation based on the FFT multislice method. *Ultramicroscopy* **2002**, *90*, 71−83.
(42) Delhaes, P. Graphite and Precursors. CRC Press. Taylor & Francis Group, *A Science Publishers Book*, 2001, ISBN 978−90−5699−228−6.
(43) Watanabe, K.; Jinnai, B.; Fukami, S.; Sato, H.; Ohno, H. Shape anisotropy revisited in single-digit nanometer magnetic tunnel junctions. *Nat. Com.* **2018**, *9*, 663.
(44) Mulazzi, M.; Chainani, A.; Takata, Y.; Tanaka, Y.; Nishino, Y.; Tamasaku, K.; Ishikawa, T.; Takeuchi, T.; Ishida, Y.; Senba, Y.; Ohashi, H.; Shin, S. Temperature dependence of the exchange stiffness in FePd(001) thin films: Deviation from the empirical law. *Phys. Rev. B* **2008**, *77*, 224425.
(45) Sakamaki, M.; Amemiya, K. Nanometer-resolution depth-resolved measurement of florescence-yield soft x-ray absorption spectroscopy for FeCo thin film. *Rev. Sci. Instrum.* **2017**, *88*, 083901.
(46) Amemiya, K.; Toyoshima, A.; Kikuchi, T.; Kosuge, T.; Nigorikawa, K.; Sumii, R.; Ito, K. Commissioning of a Soft X-ray Beamline PF-BL-16A with a Variable-Included-Angle Varied-Line-Spacing Grating Monochromator. *AIP Conf. Proc.* **2009**, *1234*, 295−298.
(47) See http://fujitsu.com/global/about/resources/news/press-releases/2015/0324-01.html for Fujitsu Ltd.
(48) Naganuma, H.; Sato, H.; Ikeda, S.; Endoh, T. Micromagnetic simulation of the temperature dependence of the switching energy barrier using string method assuming sidewall damages in perpendicular magnetized magnetic tunnel junctions. *AIP Adv.* **2020**, *10*, 075106.
(49) Weinan, E.; Weiqing, R.; Eijnden, E. V. String method for the study of rare events. *Phys. Rev. B* **2002**, *66*, 052301.

https://doi.org/10.1021/acsnano.1c09843
ACS Nano 2022, 16, 4139−4151

(50) Ren, W. E. W.; V.-Eijnden, E. Energy barriers to magnetization reversal in perpendicularly magnetized thin film nanomagnets. *J. Appl. Phys.* **2003**, *93*, 2275.

https://doi.org/10.1021/acsnano.1c09843
ACS Nano 2022, 16, 4139−4151